Electron Cyclotron Current Drive and Suprathermal Electron Dynamics in the TCV Tokamak

S. Coda, S. Alberti, P. Blanchard, T.P. Goodman,
M.A. Henderson, P. Nikkola, Y. Peysson† and O. Sauter

Centre de Recherches en Physique des Plasmas, Association
EURATOM-Confédération Suisse, Ecole Polytechnique Fédérale de Lausanne, CRPP
- EPFL, CH-1015 Lausanne, Switzerland
† Département de Recherches sur la Fusion Contrôlée, Association EURATOM-CEA,
CEA/Cadarache, 13108 Saint Paul-lez-Durance Cédex, France

E-mail: `stefano.coda@epfl.ch`

Abstract. Electron cyclotron current drive (ECCD) is an important prospective tool for tailoring the current profile in next-step devices. To fill the remaining gaps between ECCD theory and experiment, especially in the efficiency and localization of current drive, a better understanding of the physics of suprathermal electrons appears necessary. On TCV, the fast electron population is diagnosed by a multichordal, spectrometric hard X-ray camera and by a high field side ECE radiometer. The main modeling tool is the quasilinear Fokker-Planck code CQL3D, which is equipped with a radial particle transport model. Systematic studies of fast electron dynamics have been performed in TCV with modulated or pulsed electron cyclotron power, followed by coherent averaging, in order to identify the roles of collisional relaxation and radial transport in the dynamics of the suprathermal population. A consistent picture is emerging from experiment and modeling, pointing to the crucial role of the radial transport of suprathermal electrons in the physics of ECCD.

1. Introduction

Electron cyclotron current drive (ECCD) is an important tool for current profile shaping in magnetically confined plasmas, thanks to the highly localized power deposition of the EC wave and the ease of external control of its deposition location and wave-number spectrum [1, 2]. The strong influence exerted in turn by the current profile shape on the stability of the plasma to MHD modes, as well as on its confinement properties, motivates much current ECCD research. In experimentally relevant plasma conditions, the EC waves propagate from vacuum or air to the resonance layer in the plasma without encountering any cutoff, allowing the launching structures to be placed far from the harsh plasma environment, as may be necessary in a reactor.

The development of high power, high frequency, long pulse gyrotron sources in recent years has provided the fusion community with a versatile and mature technology for next-step thermonuclear fusion devices [3, 4]. The TCV tokamak (R=0.88 cm, a=0.25 cm, I_p ≤1 MA, B_ϕ ≤1.54 T) is equipped with a 4.5 MW EC heating system, powered by six second harmonic (X2, 82.7 GHz) and three third harmonic (X3, 118 GHz) 0.5 MW gyrotrons. An extremely flexible EC beam delivery system, allowing real-time poloidal and toroidal steering, matches the equally flexible plasma position and shape control system of TCV [5].

ECCD experiments have been performed in TCV with the X2 system, for a total delivered power of up to 2.8 MW, in a wide variety of plasma shapes, with a broad range of parallel wave numbers and heating locations. In particular, steady-state, fully non-inductive discharges sustained entirely by ECCD and bootstrap current are routinely obtained in TCV [6, 7, 8].

The high energy electron population created by ECCD is diagnosed primarily with a hard X-ray (HXR) pinhole camera, on loan from Tore Supra, and with a high field side electron cyclotron emission (ECE) system. HXR bremsstrahlung emission is detected by a linear array of CdTe detectors [9] along 14 chords that cover the outboard half of the cross section. The radial resolution is approximately 2 cm on the midplane and the energy resolution is approximately 7 keV [10]. Spectral pulse height analysis is performed, and eight energy bins are available for each chord with adjustable thresholds within the 10–200 keV range.

The second harmonic X-mode ECE radiometer observes the plasma along one of three possible horizontal viewlines, two on the high field side and one on the low field side, and operates in the 78–114 GHz range with 24 channels of 0.75 GHz bandwidth [11]. The EC radiation observed on the high field side is dominated by relativistically downshifted emission by the high energy end of the electron distribution function and can thus be employed to diagnose the suprathermal population [12]. The results discussed in this paper were obtained exclusively with the high field side viewlines.

The quasilinear Fokker-Planck code CQL3D [13] is employed to model the dynamics of the electron distribution function. The code is coupled to the TORAY-GA ray-tracing module [14] and solves the Fokker-Planck equation in two velocity

and one spatial dimensions. The equation includes a quasilinear EC wave damping term, a relativistic collision operator and a model for radial diffusion, with an optional dependence on the parallel velocity, a radial dependence and a particle-conserving advection term.

A concerted application of these diagnostic and numerical tools in a variety of experimental scenarios involving ECCD has generated significant evidence that cross-field transport of suprathermal electrons plays a fundamental role in ECCD physics in TCV, as will be discussed in the remainder of this article. An initial discrepancy between the predicted and measured ECCD efficiencies has been resolved by the introduction in CQL3D of a suprathermal electron diffusion coefficient of the order of the thermal diffusivity [15]. This also brings the predicted HXR emission close to the experimental measurements, whereas gross disagreement is registered without diffusion. Finally, direct experimental evidence of radial transport is obtained from time-resolved HXR and ECE measurements in studies with modulated and pulsed ECCD.

2. ECCD and suprathermal electrons

Current drive by electron cyclotron waves is theoretically predicted to operate on electrons traveling at substantially suprathermal velocities [16, 17]. Experimental measurements have confirmed that ECCD is accompanied by the creation and sustainment of a significant suprathermal population. Unmistakable suprathermal features are observed when the EC toroidal injection angle Φ is larger than $\sim$10–12°, i.e. when the parallel wave number is finite, as required for ECCD: the HXR spectral distribution deviates from that of a Maxwellian plasma, and both the HXR photon temperature (calculated from an exponential fit to the high energy component of the spectrum) and the ECE radiative temperature are well in excess of the bulk plasma temperature measured by Thomson scattering [11, 18, 19]. By contrast, with $\Phi \simeq 0$ (pure heating mode) the three temperatures coincide. (In this article Φ is defined as the angle between the EC beam and its projection on the poloidal plane at the launcher, and is positive for co-ECCD.)

The dependence of the suprathermal population on the toroidal injection angle is clearly demonstrated by figure 1, which shows the effect of sweeping Φ during a plasma discharge on two out of three launchers: while the bulk temperature and the lower energy HXR signal remain constant, the high energy HXR emission and the ECE radiative temperature increase rapidly with Φ [19]. This example also illustrates the high degree of external control of multiple deposition locations and toroidal injection angles available on TCV, which has proven instrumental in the application of ECCD to current and pressure profile tailoring [5, 6, 7, 20, 21].

The presence of a suprathermal electron population created by X2 ECCD has also been shown to engender enhanced absorption of the X3 waves over that expected for a Maxwellian plasma [22].

As figure 1 shows, the energy resolved HXR measurement is a particularly sensitive
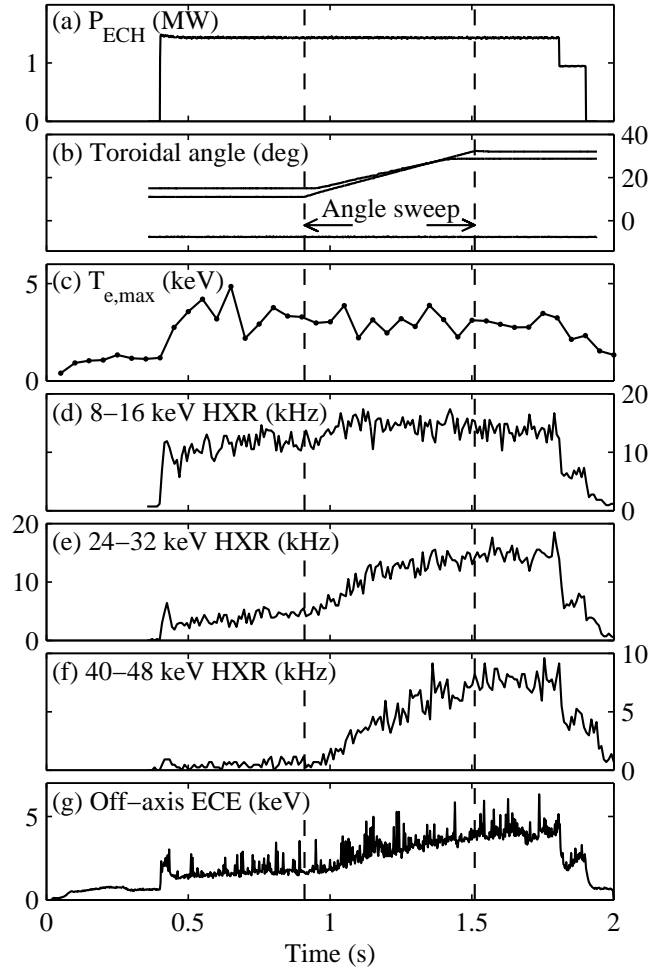
Figure 1. TCV discharge 22035 (limiter configuration, plasma current I_p=310 kA, line-averaged density $\bar{n}_e$=1.5×10^{19} cm^{-3}, edge elongation κ_{edge}=1.4), featuring a sweep of the EC toroidal injection angle on two out of three launchers (from 11 to 32° and from 15 to 29°, respectively): (a) total EC power, (b) toroidal angles of the three launchers (positive for co-ECCD), (c) peak electron temperature, (d–f) three energy channels of the HXR signal on a central chord (in units of 10^3 counts/s), (g) ECE radiative temperature on an off-axis channel.

indicator of the relative dynamics of the thermal and suprathermal components. On the other hand, photon statistics in this spectral range tend to limit the intrinsic temporal resolution of the measurement [9]. The ECE diagnostic, by contrast, offers the advantage of good time resolution. However, the interpretation of ECE data is complicated by the fact that a given emission frequency corresponds to a continuum of spatial positions and electron energies, since the EC frequency depends, relativistically, on both magnetic field and energy. To deconvolve the two quantities some constraints must be applied. The approach that has shown the most promise is based on the assumption of a bi-Maxwellian electron distribution function, describing the bulk and suprathermal populations. This assumption is qualitatively supported by both HXR

data and CQL3D modeling. By then applying constraints on the profile shapes for the suprathermal density and temperature, the absolute values of these quantities can be derived from the ECE data [11].

3. Suprathermal electron dynamics: the role of spatial transport in ECCD

The physical underpinnings of electron cyclotron resonance heating (ECRH), particularly the power absorption and the power deposition profile, have been validated by numerous experimental measurements [23, 24]. Predictions for current drive have also been tested experimentally, with less uniform results: while good agreement with Fokker-Planck quasilinear theory is obtained in some devices [25], discrepancies remain in other cases. In particular, ECCD efficiency in TCV has been generally grossly overestimated by quasilinear theory, which predicted strong nonlinear enhancement by the unusually large EC power densities achieved [15]. On the other hand, the driven current is underestimated by factors ranging from 1 to 3 [26] by linear calculations performed by TORAY-GA, based on the Cohen model [27] which neglects nonthermal effects as well as the current excited in the thermal portion of the electron distribution by electron-electron collisions.

The key to resolving these discrepancies must lie in the dynamics of the suprathermal electron population that governs the physics of ECCD. In particular, cross-field transport of the high energy current carriers would tend to reduce their local density and correspondingly limit the nonlinear enhancement of the current drive efficiency. In TCV we have studied the suprathermal electron dynamics both by direct experimental measurements and by numerical simulations, culminating in crucial comparisons between the two.

3.1. Experimental measurements

The spatially resolved, line-integrated HXR measurement can be inverted by various techniques to provide a measure of the local emissivity under the assumption of poloidal uniformity. A systematic study of the inverted profiles in different ECCD aiming geometries and plasma conditions reveals a complex phenomenology which is beyond the scope of the present article. Here we shall focus on two nearly universal observations for toroidal injection angles larger than 20°, which have strong implications for the topic under discussion. Firstly, with predominantly central deposition the inverted profiles are broader than the theoretical power deposition profile calculated by either TORAY-GA or CQL3D (which are invariably in good agreement). Secondly, with predominantly off-axis deposition, up to $\rho=0.5$, the inverted profiles are centrally peaked. (In this paper ρ is a normalized flux-surface coordinate proportional to the square root of the enclosed volume.)

These observations are exemplified by figure 2. The HXR emission profiles are clearly very different from, and in particular much broader than, the power deposition
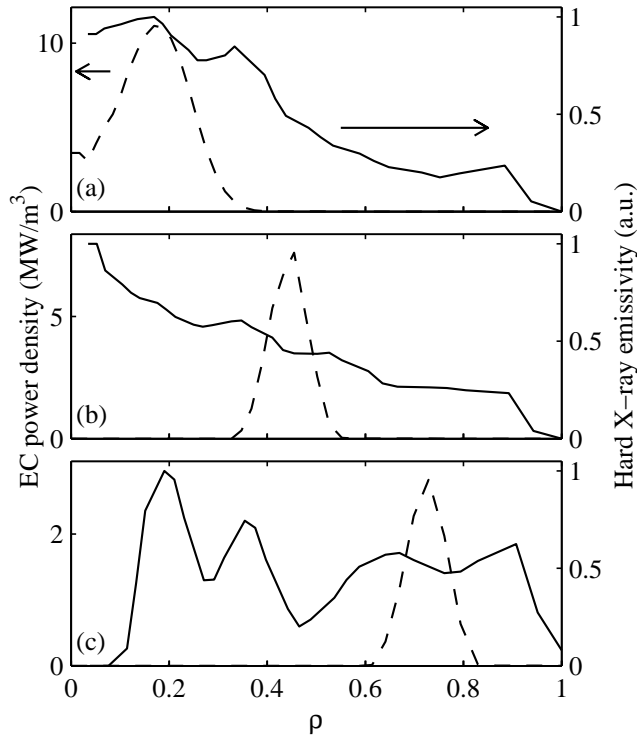
Figure 2. TCV discharges (a) 21982, (b) 21991 and (c) 22003: hard X-ray emissivity profiles (solid lines), derived with the Fischer regularization method from the line-integrated profiles averaged from 0.67 to 1.12 s; EC power density profiles (dashed lines) calculated by ray tracing. The total injected power is 1.15 MW, with 100% calculated first-pass absorption for (a) and (b) and 62% for (c) (multiple-pass absorption near the center is estimated to be negligible in this launching geometry). The effective toroidal injection angles for all launchers are in the range 25–29°. The three cases are similar limited discharges with I_p =230–240 kA, $\bar{n}_e$=1.5–1.7×10^{19} cm^{-3}, κ_{edge}=1.5–1.6.

profiles. Suprathermal electrons thus exist in regions in which the theoretical EC power deposition is negligible; thus, either the deposition profile is highly anomalous, i.e. departs greatly from the theoretical predictions, or a mechanism must exist for transporting fast electrons far from the deposition region. The former hypothesis is in disagreement with a large body of evidence showing that ray tracing accurately predicts the EC power deposition [23, 24], including specific recent estimations in TCV using modulation techniques [28]. These data thus indicate that transport plays a significant role in determining the suprathermal electron distribution at toroidal injection angles > 20° and power densities in excess of 2 MW/m^3.

While the similarity of the emission profiles in figure 2(a) and (b) appears to suggest a possible profile resilience scenario, figure 2(c) shows that when the EC waves are deposited at sufficiently large radii the central emissivity falls to zero.

It is important to note that the main features of the profiles, i.e. their widths and the locations of the main peaks, are not dependent on the details of the profile inversion, and can be readily identified directly in the line-integrated profiles, as shown in
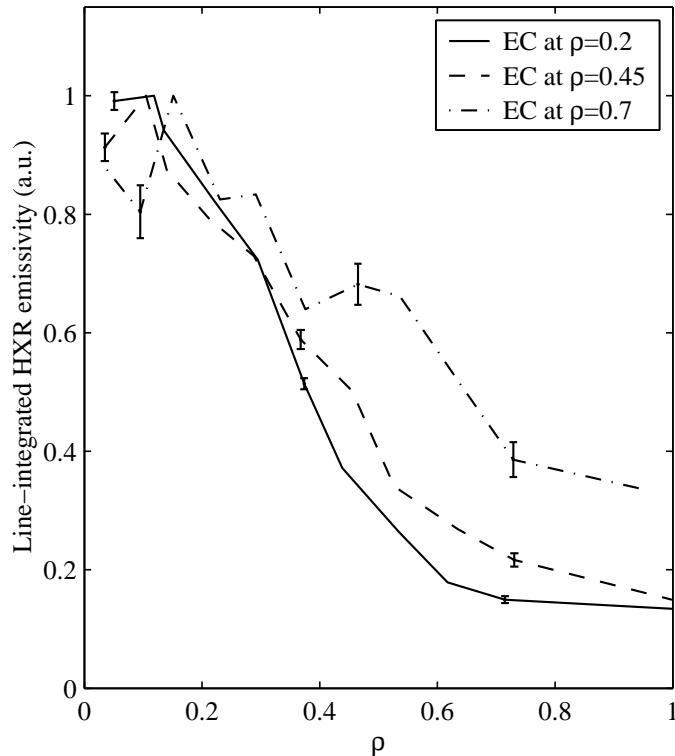
Figure 3. Line-integrated hard X-ray emission profiles for TCV discharges 21982 (solid line), 21991 (dashed line) and 22003 (dash-dotted line), averaged over 0.45 s, as a function of the minimum normalized radius for each chord, i.e. the point of tangency to the flux surface. The local emissivity profiles shown in figure 2 are derived from these data.

figure 3. While minor features of the inverted profiles, particularly the secondary peaks or plateaus, are in some cases not significant within the statistical uncertainties (shown on the integrated profiles), emissivity distributions as narrow as the EC power deposition profiles would clearly be incompatible with the measured line-integrated profiles.

The dynamics of suprathermal electrons are governed by several competing diffusive processes: collisional relaxation in velocity space (slowing-down and pitch-angle scattering), quasilinear rf diffusion in velocity space, and anomalous turbulence-driven transport in real space. There is no "source", since the heating process itself is of a diffusive nature (albeit not energy conserving). In general, the dynamics will be dominated by the shortest relaxation time in the system. To illustrate the potential effect of radial transport in TCV, let us adopt the common assumption that the relevant time scale is the collisional slowing-down time τ_{SD}; in this case the effect of a radial diffusion coefficient D will be to broaden the fast electron profile by

$$\Delta w \sim (D\tau_{\mathrm{SD}})^{1/2}. \tag{1}$$

As an example with typical central parameters for TCV discharges with ECCD ($n_e=2\times10^{19}$ m^{-3}, $T_e=5$ keV, effective ion charge $Z_{\mathrm{eff}}=4$), a diffusivity of the order of the bulk thermal diffusivity, $D \sim 3$ m^2/s, would broaden a 120 keV population profile in TCV

plasmas by 12 cm, i.e. one-half the minor radius. Clearly, identical parameters would produce a less noticeable effect in a larger tokamak. It must be noted, however, that D has been generally estimated to be between 0.3 and 1.0 m^2/s for the suprathermals sustained by lower hybrid current drive, with the exception of JET (where an estimate of $D \sim 6$–10 m^2/s was given) [29].

A direct experimental measurement of the rate of transport of suprathermal electrons presents formidable difficulties, as was already documented in the long history of lower hybrid current drive experiments [29, 30, 31, 32]. Some related studies with EC waves were reported in [33, 34]. Since several potentially overlapping time scales are at play, an unambiguous determination of the complete system dynamics is difficult to conceive under controlled experimental conditions. On TCV, we have adopted the approach of applying multiple techniques aimed at providing progressively stronger constraints on these dynamics.

Two such techniques have been employed recently to exploit the specific characteristics of the HXR and ECE diagnostics, respectively. Square-wave modulation of the electron cyclotron power has been performed in order to enhance the photon statistics and thus the temporal resolution of the HXR camera by coherent averaging. Photon statistics also dictated high power levels (typically 2.25 MW with 50% duty cycle), which resulted in strong modulation of the bulk plasma parameters, particularly the density and the temperature (see figure 4). Since the electron energy confinement time is of the same order as the slowing-down time for electrons travelling at 5 to 8 times the thermal velocity, a separation of the relevant time scales becomes impossible.

However, information on the suprathermal dynamics is contained in the temporal evolution of the *spectral distribution* of the HXR signals. If the slowing-down time is much shorter than the characteristic diffusion time, the spectra must be determined by local properties, with no effective communication over distant regions in space. Heating is applied to different velocity classes in different spatial regions, because of the Doppler shift needed to match the resonance condition locally. Additionally, the physical parameters that govern the steady-state distribution function, i.e. the EC power density, the bulk plasma density and the bulk electron temperature, are all spatially varying functions. Therefore the resulting spectral distribution should not be spatially uniform in general. However, in the relaxed state we invariably find that the spectral shape is essentially constant in space, even well outside the theoretical deposition region (albeit at much lower amplitude) [35]; this is most naturally interpreted as an equilibration resulting from radial transport, but could also indicate an anomalous deposition profile in both physical and velocity space.

These dynamical measurements have shown for the first time that this uniformity is not present immediately after switch-on: as shown in figure 5(a) for a case with central co-ECCD (Φ=25°), the signal from a central chord is initially larger than the off-axis signal at low energy, while their roles are reversed at high energy. The on-axis spectrum does not change appreciably over time, whereas the off-axis spectrum becomes similar to the former over a period of approximately 10 ms. A corresponding relaxation of the
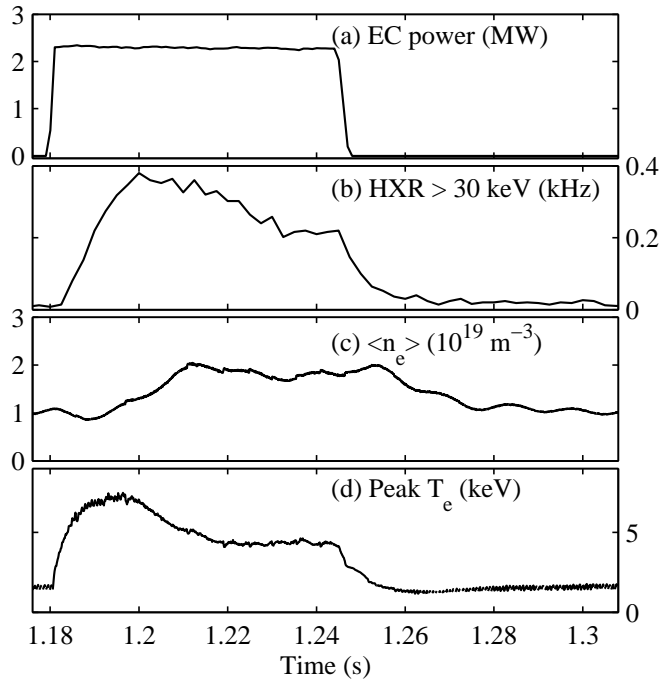
Figure 4. TCV shot 21978 (limiter configuration, I_p =240 kA, κ_{edge}=1.5–1.6): time histories, during one EC modulation period (Φ=25°), of (a) EC power, (b) HXR emission along a central chord for photon energies larger than 30 keV, (c) line-averaged electron density, (d) peak electron temperature.

photon temperature profile towards a flat profile is seen in figure 5(b) [19]. If we assume that the relaxation is of a diffusive nature, we can deduce from the observed relaxation time a lower bound ∼1.5 m²/s for the diffusivity in this discharge.

The higher sensitivity of the ECE system is compatible with perturbative studies. In a second experiment, we have applied short periodic ECCD pulses to the plasma and studied the ECE response by coherent averaging. Pulses longer than 0.3 ms were seen to result in a first peak, followed by a descent and a further increase until the end of the pulse, indicating that the pulse length exceeded the characteristic rf diffusion time. To avoid this complicating effect, the pulse was thus kept to a length of 0.25–0.3 ms. The applied power was 0.45–0.9 MW with a period of 10 ms, therefore a 3% duty cycle and an average power <27 kW, too low to affect the plasma parameters measurably.

Two examples, both with central ECCD, are shown in figure 6, with the plasma and ECE radiometer geometries shown in figure 7. In the case of figure 7(a) the ECE chord traverses the plasma center, whereas in the case of figure 7(b) the smallest normalized minor radius accessed by ECE is approximately 0.55. In both cases the time to peak increases with the ECE frequency, as shown in figure 8. Moreover, the time lags are clearly larger when the ECE radiometer is aimed off-axis: indeed, when plotted versus the cold-resonance ρ, the two curves connect smoothly to each other [figure 8(II)].

The cold-resonance radial coordinate in figure 8(II) is to be taken only as a guiding
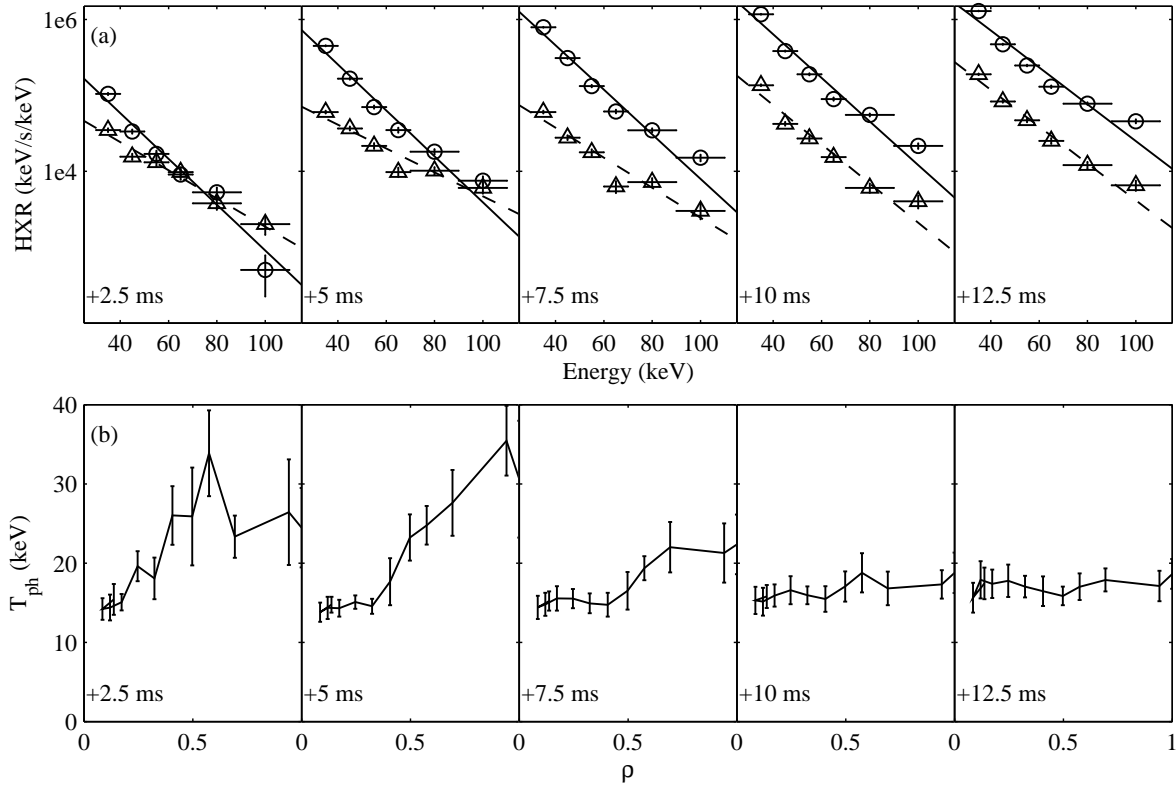
Figure 5. TCV shot 21978 (cf. figure 4): (a) HXR emission (in units of power per photon energy interval) as a function of energy in 5 snapshots after the ECCD switch-on (t=0), for a central (circles, solid line) and an off-axis (triangles, dashed line, $\rho \sim 0.6$) chord; (b) spatial profiles of the photon temperature for the same snapshots (ρ here indicates the minimum normalized radius for each chord, i.e. the point of tangency to the flux surface) [19].

parameter: indeed, in the presence of a substantial suprathermal tail, an increase in frequency can be associated either to a shift towards the high field side (larger minor radius) or to an increase in electron energy. However, for equal energy and frequency, the signals from the two chords originate in different spatial regions. Thus this observation corroborates the hypothesis that a transport mechanism is at play and that a non-negligible fraction of the fast electrons generated by ECCD is transported far from the deposition region. A more quantitative analysis will require modeling. In particular, the time lag will generally depend on both the slowing-down time and the diffusion time: therefore the detailed dependence of the time lag on the frequency cannot uniquely provide quantitative information on the diffusion coefficient. The time to peak is, however, only one parameter of the dynamical response. The full dynamics, particularly the decay time, can provide strong constraints on the modeling. Further work is planned in this direction.
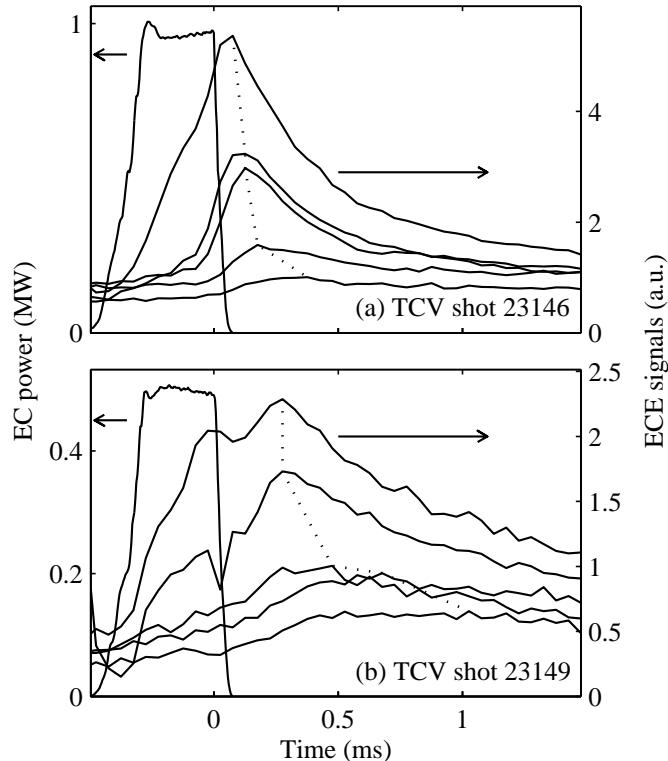
Figure 6. Response of selected ECE signals to a short central ECCD pulse (ending at $t=0$), averaged over 170 coherent pulses; the ECE frequency increases as the peak moves to later times: (a) ECE radiometer on the midplane, (b) ECE radiometer off-axis ($\rho > 0.55$). (See geometry in figure 7.) The plasma conditions are similar in the two discharges: limiter configuration, $I_p = 240$ kA, $\bar{n}_e = 1.7$–1.8×10^{19} cm^{-3}, $T_{e,\mathrm{max}} = 1.6$–1.7 keV, $\kappa_{\mathrm{edge}} = 1.4$–1.5. The EC power in case (a) is twice the power in case (b).

3.2. Quasilinear Fokker-Planck modeling

The discrepancies between theory and experiment on the ECCD efficiency, mentioned at the beginning of this section, have been resolved by adjusting the diffusion coefficient in the Fokker-Planck code CQL3D, with optional dependences on the radial location and on the parallel velocity [15]. When D is of the order of the bulk thermal diffusivity, the distribution of current-carrying fast electrons is broadened and nonlinear enhancement is strongly inhibited; with $D \sim 3$–5 m^2/s, the experimentally measured EC-driven current can generally be reproduced. The same level of diffusivity does not change the predicted efficiency significantly in experimental situations in which nonlinear enhancement is not expected [15]. Thus a unifying picture is beginning to emerge.

The achievement of fully non-inductive discharges driven entirely by off-axis ECCD and bootstrap current [5, 20, 21] is a striking illustration of the effect of this suprathermal transport. The value of D in the center (D_0) having been set such as to match the total driven current, the EC-driven current profile calculated by CQL3D is centrally peaked in spite of the power being deposited approximately at half-radius [36], as illustrated by
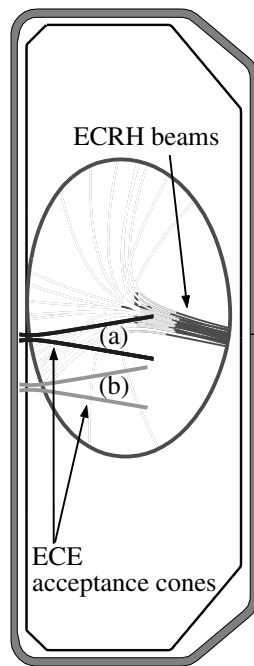
Figure 7. Geometries of ECRH launching and ECE radiometry for the two cases shown in figure 6 (in reality the radiometer is fixed and the plasma and EC beams are moved). The lighter grey portion of the beams denotes the region of 99% absorption.
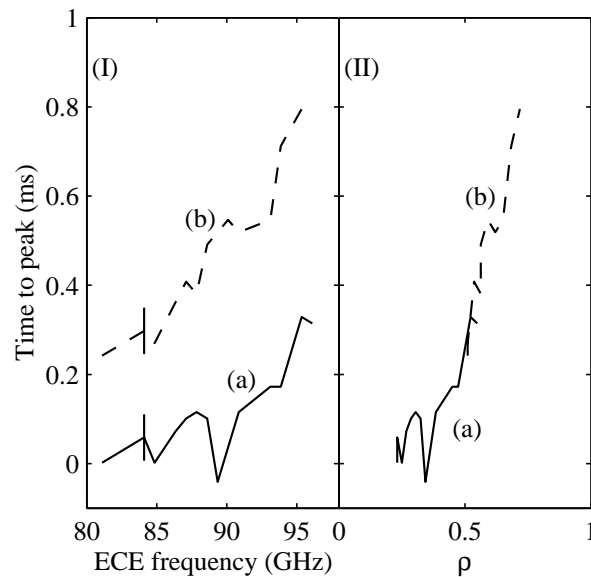

Figure 8. Time lag from the end of the ECCD pulse to the ECE peak, for the two cases (a) and (b) shown in figure 6, (I) as a function of ECE frequency, (II) as a function of the equivalent ρ at the cold resonance.
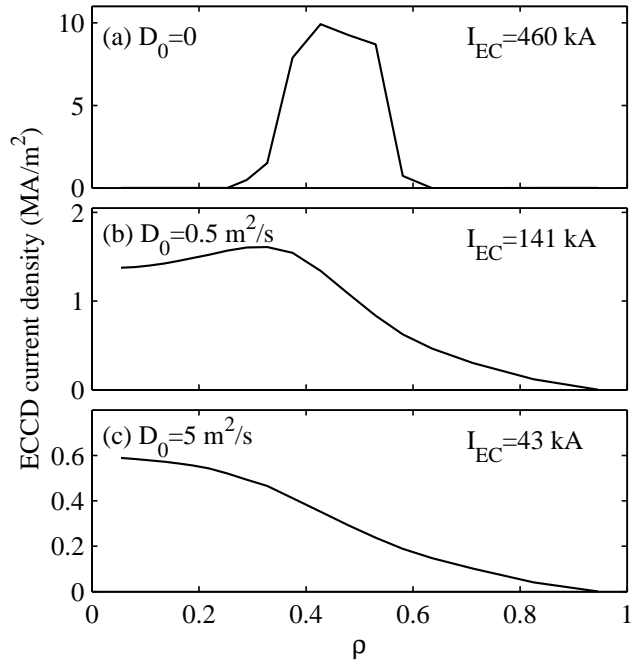
Figure 9. (a)–(c) EC-driven parallel current density profiles calculated by CQL3D for TCV discharge 21657 at 1.8 s (limiter configuration, I_p =72 kA, $\bar{n}_e$=5.1×10^{18} cm^{-3}, $T_{e,\text{max}}$=3.3 keV, κ_{edge}=1.6), fully sustained by 0.9 MW off-axis co-ECCD (Φ=21°), for three values of the central diffusivity D_0 (0, 0.5, 5 m^2/s), yielding different values of the EC-driven current (respectively 460, 141, 43 kA); the current in case (c) matches the experimental measurement, since the bootstrap current $I_p - I_{EC}$ is 29 kA [37]. Linear calculations yield a driven current of 17 kA. The power deposition profile is similar to the calculated current profile in (a) and peaks at ρ=0.45. A radial L-mode-like dependence is assumed for D, yielding a local diffusivity of 7 m^2/s in case (c) at the deposition location; D is assumed to be independent of velocity.

figure 9 [37]. (It should be noted that the total current profile is nevertheless calculated to be hollow, owing to a large off-axis bootstrap current contribution.) In this case, D has been taken to be independent of the parallel velocity and to increase with radius according to L-mode scaling [36]; in particular, at the EC power deposition location D equals approximately 7 m^2/s. It is important to note that even in the presence of this radial diffusion, the total driven current (43 kA) remains larger than that predicted by linear theory (17 kA).

When the loop voltage is nonzero, CQL3D calculates the sum of the Ohmic and EC-driven current self-consistently taking into account the effect of the electric field. This current is then compared to the measured total current minus the bootstrap current (calculated from pressure profile measurements by Thomson scattering). This procedure is hampered by limited accuracy in the Ohmic component, which can be ascribed in particular to uncertainties in Z_{eff} [38]. For this reason, fully non-inductive discharges in which the Ohmic current is zero provide an especially strong constraint to the modeling. Nevertheless, the need for a finite diffusion coefficient is readily apparent
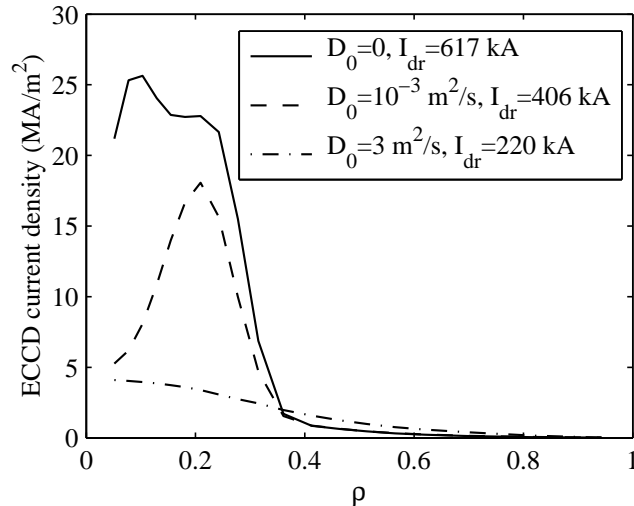
Figure 10. Externally driven (EC + Ohmic) parallel current density profiles calculated by CQL3D for the centrally heated TCV discharge 21982 at 1.0 s (limiter configuration, I_p =240 kA, $\bar{n}_e$=1.5×10^{19} cm^{-3}, $T_{e,\max}$=3.5 keV, κ_{edge}=1.5; EC power = 1.13 MW, Φ=25°), for three values of the central diffusivity D_0 (0, solid curve; 0.001 m^2/s, dashed curve; 3 m^2/s, dash-dotted curve), yielding different values of the current (respectively 617, 406, 220 kA); the current in the last case matches the experimental measurement. The power deposition profile is similar to the calculated current profile in the D_0=0 case; D is assumed to be independent of velocity.

also in discharges with a nonzero loop voltage, as shown in figure 10 for a centrally heated case.

To gain further insight into the physics of ECCD at the high power densities of TCV, it is instructive to compare the calculated parallel current density distributions in velocity space with and without diffusion. The differential densities $dj/d|v_\parallel|$ and $dj/dv_\perp$ (where $\parallel$ and $\perp$ are relative to the total magnetic field) are plotted in figure 11 for the same non-inductive discharge of figure 9. Here, $dj/d|v_\parallel| = -e|v_\parallel| \int_0^\infty 2\pi \left[f(v_\perp, |v_\parallel|) - f(v_\perp, -|v_\parallel|) \right] v_\perp dv_\perp$, and $dj/dv_\perp = -2\pi e v_\perp \int_{-\infty}^\infty f(v_\perp, v_\parallel) v_\parallel dv_\parallel$, where $f(v_\perp, v_\parallel)$ is the electron distribution function. The average energy of the current-carrying electrons decreases from ∼70–100 times the thermal energy in the case of no diffusion to ∼15–35 times the thermal energy with D_0=5 m^2/s.

The effectiveness of diffusion in broadening the spatial distribution of fast electrons is enhanced at the high energies to which these electrons are accelerated by the high-power EC waves: since the slowing-down time increases with velocity as v^3, the broadening Δw, according to equation (1), increases as $v^{3/2}$. By applying equation (1) to the discharge of figure 11, with parameters n_e= 6×10^{18} m^{-3}, T_e=1.6 keV, Z_{eff}=3, D=7 m^2/s at the deposition location, an electron energy of 80×T_e=130 keV results in $\Delta w \simeq$21 cm, i.e. a broadening of the order of the radius of the plasma column. This is of course only an approximate upper bound: since transport itself acts to reduce the average electron energies, as demonstrated by figure 11, the width of the relaxed fast
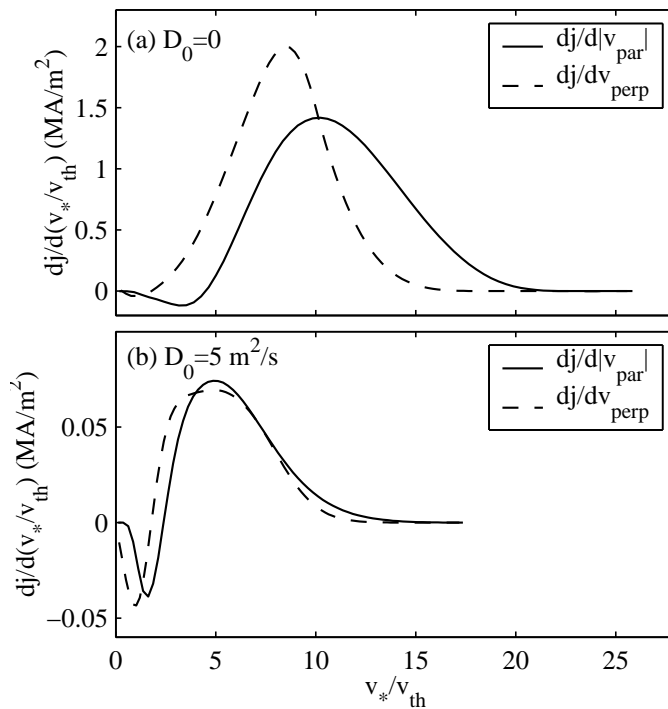
Figure 11. Differential parallel current densities in velocity space, $dj/d|v_\parallel|$ (solid curves) and $dj/dv_\perp$ (dashed curves), calculated by CQL3D for TCV shot 21657 at 1.8 s (cf. figure 9): (a) $D_0=0$, (b) $D_0=5$ m^2/s. In the abscissa v_* denotes $|v_\parallel|$ and $v_\perp$, respectively, for $dj/d|v_\parallel|$ and $dj/dv_\perp$.

electron profile will be smaller than that given by this estimate. However, this example serves to illustrate the important concept that the ECCD spatial broadening increases inherently with power simply by virtue of the longer lifetimes of the current carriers, even in the absence of any direct power degradation, i.e. even if D is independent of power. Longer lifetimes also imply increased current drive losses [39]. It should be noted that in a future reactor-scale tokamak such as ITER the large machine size would result both in a reduced power density and in an increased device scale length, rendering the nonlinear broadening negligible for all practical purposes.

Different forms of functional dependence of the diffusivity on the parallel velocity, derived from different models of electrostatic or magnetic turbulence, have been employed in CQL3D, with no conclusive evidence thus far in favor of one or the other [38]. The reason for this can be gleaned from figure 11: different models will give similar results provided the value of the diffusivity is approximately the same in the current-carrying region of velocity space.

A remarkable similarity is observed between the current distributions in the parallel and perpendicular velocities. On the low field side of the nominal resonance, electrons that resonate with EC waves of finite parallel wave number possess suprathermal *parallel* velocities; the wave-particle interaction, on the other hand, acts to increase the *perpendicular* velocity. The simulations show that the combination of the two effects
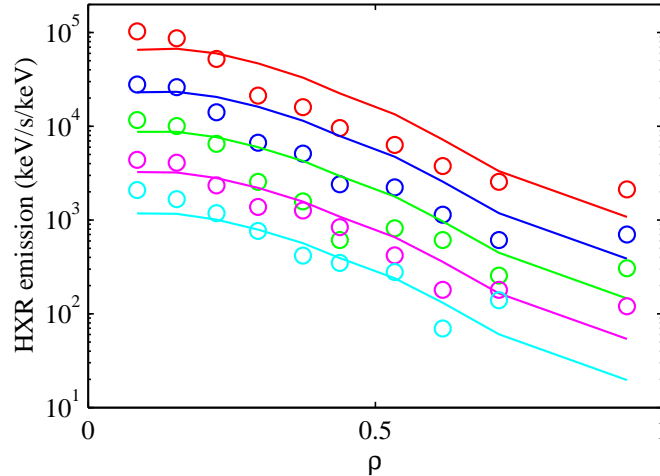
Figure 12. TCV shot 19285 (0.45 MW central co-ECCD, Φ=13°; limiter configuration, I_p=205 kA, $\bar{n}_e$=1.8–1.9×10^{19} cm^{-3}, $T_{e,\mathrm{max}}$=3 keV, κ_{edge}=1.3): measured HXR emission averaged from 0.3 to 0.5 s (circles) vs. that predicted by CQL3D at 0.45 s (curves), as a function of chordal spatial location (minimum normalized radius) for 5 energy channels of 8 keV width in the 16–56 keV range (descending amplitude for increasing energy) [19]. The value of D_0 is adjusted in CQL3D to reproduce the experimental current and is equal to 3 m^2/s; D is assumed to be independent of velocity.

results in a current distribution that is approximately symmetric in $|v_\parallel|$ and $v_\perp$ (a considerable weaker symmetry, however, than complete pitch-angle isotropy, which is certainly not satisfied).

3.3. Comparison of calculated and measured HXR emissivities

A further approach to studying the suprathermal electron relaxation phenomena consists of direct comparisons of HXR data with the bremsstrahlung emission predicted by the CQL3D code for the specific geometry of our diagnostic. Once the diffusion coefficient is adjusted to permit the code to match the total driven current, in discharges with central deposition the calculated emission is in good agreement with the measurements [15, 19, 38], generally within a factor of 3 everywhere, as exemplified by figure 12. With off-axis deposition, calculations tend to underestimate the emissivities by factors up to 6–8 [36, 38]; however, the spectral distribution generally remains in good agreement.

Without radial transport, not only is the predicted current much too large, the predicted HXR signal is also far narrower spatially than the measured one, as shown in figure 13(a). In particular, these results provide strong evidence that the spatial uniformity of the spectral shape is a consequence of spatial transport. The shape is parametrized in figure 13(b) by a photon temperature, which is seen to be a strong function of minor radius in the case D_0=0, whereas with D_0=3 m^2/s a uniform temperature is recovered, which is moreover in excellent quantitative agreement with the experimental values. Note that in the diffusionless case the calculated photon
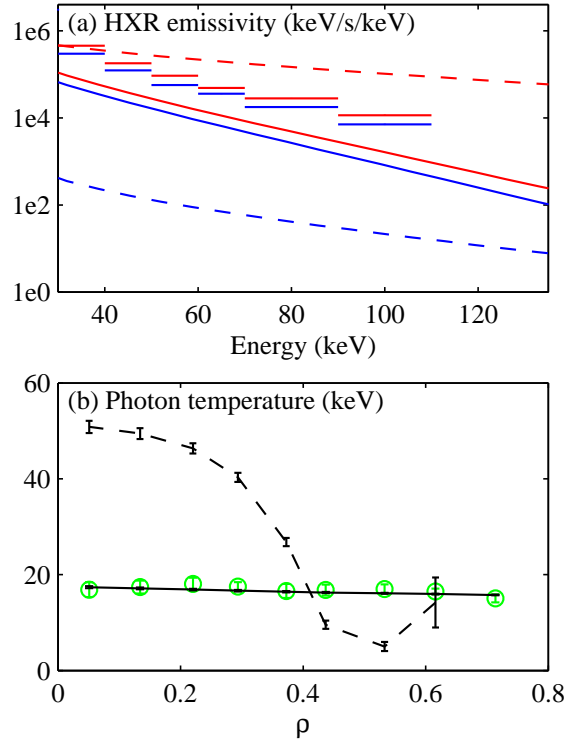
Figure 13. TCV shot 21982 (cf. figure 10): (a) HXR emissivity spectrum for a central chord (red) and a chord with a minimum $\rho \sim 0.37$ (blue): experimental data averaged from 0.65 to 1.35 s (horizontal bars), CQL3D calculations at 1.0 s with diffusivity $D_0=3\,\mathrm{m}^2/\mathrm{s}$ (solid curve) and $D_0=0$ (dashed curves); (b) photon temperature calculated from an exponential fit to the spectra in the interval 30-120 keV, as a function of radial position ρ (minimum normalized radius for each chord): experimental data (green), CQL3D data with $D_0=3$ m^2/s (solid black curve) and $D_0=0$ (dashed black curve).

temperature appears to decrease with radius, whereas the opposite behavior is observed experimentally immediately after power switch-on (see figure 5). This disagreement is not significant per se, since the CQL3D calculations refer to steady-state conditions and cannot reproduce a dynamical evolution in which strong self-inductive transient electric fields are present. In addition, the calculated spectra are only approximately exponential; in particular, at higher energy the slope becomes less steep (higher temperature) at larger radii. The key observation in both the experiment (initial spectrum before diffusion has occurred) and the simulation (steady-state scenario without diffusion) is that the shape of the spectrum is not uniform in space, since all the physical quantities that determine it are indeed not uniform.

4. Conclusions and outlook

ECCD is being used on TCV as a powerful tool for current and pressure profile shaping, especially with the high degree of control afforded by fully non-inductive operation, thus in the absence of an electric field, in steady state. At the same time, TCV

is one of the premier test beds for fundamental inquiries into the physics of ECCD and the associated suprathermal electron dynamics, owing to a uniquely powerful and flexible ECH system and dedicated diagnostics, complemented by an advanced and comprehensive Fokker-Planck quasilinear code. The fundamental relaxation processes governing the suprathermal dynamics are being investigated through multiple experimental approaches and comparisons with modeling.

Strong evidence supports the conclusion that the suprathermal electrons excited by ECCD undergo cross-field transport at a rate comparable to that of thermal transport, resulting in a reduction of the nonlinear effects expected at the TCV power densities, and particularly of the attendant nonlinear enhancement of the current drive efficiency. However, in spite of this radial transport the efficiency still exceeds that predicted by linear theory, which has been shown to be fairly accurate at lower power levels [40]. A gain in efficiency is therefore still obtained by operating at higher power levels.

Much remains to be known about the underlying transport mechanism. Fokker-Planck simulations using different transport models, based on both electrostatic and electromagnetic turbulence, have thus far been inconclusive. A crucial question that must be addressed is the dependence of this transport on the ECH power density itself; it is plausible for instance to suppose a power degradation mechanism to be at play as in thermal transport, but this hypothesis has not yet been tested.

Acknowledgments

References

[1] Erckmann V and Gasparino V 1994 *Plasma Phys. Control. Fusion* **36** 1869
[2] Lloyd B 1998 *Plasma Phys. Control. Fusion* **40** A119
[3] Alberti S *et al* 2001 *Fusion Eng. Design* **53** 387
[4] Piosczyk B *et al* 2002 *Proc. 19th Int. Conf. on Fusion Energy 2002 (Lyon, 2002)* (Vienna: IAEA) CD-ROM file CT-7Rb and http://www.iaea.org/programmes/ripc/physics/
[5] Goodman T.P. *et al* 2002 *Proc. 19th Int. Conf. on Fusion Energy 2002 (Lyon, 2002)* (Vienna: IAEA) CD-ROM file OV/4.2 and http://www.iaea.org/programmes/ripc/physics/
[6] Sauter O. *et al* 2000 *Phys. Rev. Lett.* **84** 3322
[7] Coda S. *et al* 2000 *Plasma Phys. Control. Fusion* **42** B311
[8] Sauter O. *et al* 2001 *Phys. Plasmas* **8** 2199
[9] Peysson Y. and Imbeaux F. 1999 *Rev. Sci. Instrum.* **70** 3987
[10] Peysson Y., Coda S. and Imbeaux F. 2001 *Nucl. Instrum. and Methods in Phys. Res. A* **458** 269
[11] Blanchard P., Alberti S., Coda S., Weisen H. and Klimanov I. 2002 *Plasma Phys. Control. Fusion* **44** 2231
[12] TFR Group and Fidone I 1981 *Phys. Rev. A* **24** 2861

[13] Harvey R.W. and McCoy M.G. 1993 *Proc. IAEA Technical Committee Meeting on Advances in Simulation and Modeling in Thermonuclear Plasmas (Montreal, 1992)* (Vienna: IAEA) p 498

[14] Matsuda K. 1989 *IEEE Trans. Plasma Sci.* **17** 6

[15] Harvey R.W., Sauter O., Prater R. and Nikkola P. 2002 *Phys. Rev. Lett.* **88** 205001

[16] Fisch N.J. and Boozer A.H. 1980 *Phys. Rev. Lett.* **45** 720

[17] Harvey R.W., McCoy M.G. and Kerbel G.D. 1989 *Phys. Rev. Lett.* **62** 426

[18] Coda S. *et al* 1999 *Proc. 26th Eur. Conf. on Controlled Fusion and Plasma Physics (Maastricht 1999)* (European Physical Society) Europhys. Conf. Abstr. **23J** 1097

[19] Coda S. *et al* 2002 *Proc. 29th Eur. Conf. on Controlled Fusion and Plasma Physics (Montreux 2002)* (European Physical Society) Europhys. Conf. Abstr. **26B** (O-4.03)

[20] Sauter O. *et al* 2002 *Proc. 29th Eur. Conf. on Controlled Fusion and Plasma Physics (Montreux 2002)* (European Physical Society) Europhys. Conf. Abstr. **26B** (P-2.087)

[21] Sauter O. *et al* 2002 *Proc. 19th Int. Conf. on Fusion Energy 2002 (Lyon, 2002)* (Vienna: IAEA) CD-ROM file EX/P5-06 and http://www.iaea.org/programmes/ripc/physics/

[22] Alberti S. *et al* 2002 *Nucl. Fusion* **42** 42

[23] Goodman T.P. *et al* 1998, *Proc. 2nd Europhysics Topical Conf. on Radio Frequency Heating and Current Drive of Fusion Devices (Brussels, 1998)* p 245

[24] Petty C.C. *et al* 2000 *Proc. 4th Int. Conf. on Strong Microwaves in Plasmas (Nizhny Novgorod, 1999)* (Nizhny Novgorod: Russian Academy of Sciences) **1** 41

[25] Petty C.C. *et al* 2001 *Nucl. Fusion* **41** 551

[26] Nikkola P. and Sauter O. 2000 *Proc. Joint Varenna-Lausanne Int. Workshop (Varenna, 2000)* (Bologna: Editrice Compositori) Theory of Fusion Plasmas p 345

[27] Cohen R.H. 1987 *Phys. Fluids* **30** 2442

[28] Manini A. *et al* 2002 submitted to *Nucl. Fusion*

[29] Peysson Y. 1993 *Plasma Phys. Control. Fusion* **35** B253

[30] Kirkwood R. *et al* 1990 *Phys. Fluids B* **2** 1421

[31] Giruzzi G. *et al* 1995 *Phys. Rev. Lett.* **74** 550

[32] Jones S.E. *et al* 1995 *Phys. Plasmas* **2** 1548

[33] Lopes Cardozo N.J. *et al* 1993 *Proc. 14th Int. Conf. on Fusion Energy 1992 (Würzburg, 2002)* vol 1 (Vienna: IAEA) p 271

[34] Esipchuk Yu.V., Kirneva N.A., Martynov A.A. and Trukhin V.M. 1995 *Fizika Plazmy* **21** 577 [1995 *Plasma Phys. Reports* **21** 577]

[35] Coda S. *et al* 2001 *Proc. 28th Eur. Conf. on Controlled Fusion and Plasma Physics (Madeira 2001)* (European Physical Society) Europhys. Conf. Abstr. **25A** 301

[36] Nikkola P. *et al* 2002 *Proc. IAEA Tech. Committee Meeting on ECRH Physics and Technology for Fusion Devices and EC-12 (Aix-en-Provence, 2002)* (to be published)

[37] Goodman T.P. *et al* 2002 *Proc. 29th Eur. Conf. on Controlled Fusion and Plasma Physics (Montreux 2002)* (European Physical Society) Europhys. Conf. Abstr. **26B** (P-2.081)

[38] Nikkola P., Coda S., Harvey R.W. and Sauter O. 2002 *Proc. Joint Varenna-Lausanne Int. Workshop (Varenna, 2002)* (Bologna: Editrice Compositori), to be published in Theory of Fusion Plasmas

[39] Luckhardt S.C. 1987 *Nucl. Fusion* **27** 1914

[40] Petty C.C. *et al* 2002 *Proc. 19th Int. Conf. on Fusion Energy 2002 (Lyon, 2002)* (Vienna: IAEA) CD-ROM file EX/W-4 and http://www.iaea.org/programmes/ripc/physics/